Biomass Conversion and Biorefinery
https://doi.org/10.1007/s13399-023-04280-z

ORIGINAL ARTICLE

Synthesis of Fe_3O_4@SiO_2@α-Fe_2O_3/TiO_2-rGO nanohybrids for heterogeneous photocatalytic transformation of lignocellulosic biomass

Sudip Baral[1] · Chunjie Xia[1] · Ishani M. Senanayake[2] · Haoran Yang[1] · Elise Jinon[3] · Cole Cameron[1] · Boyd M. Goodson[2,4] · Yuhong Qin[5] · Jia Liu[1,4]

Received: 6 December 2022 / Revised: 15 April 2023 / Accepted: 25 April 2023

Abstract

This study explored mild and cost-effective conditions for the valorization of lignocellulosic biomass. Herein, reduced graphene oxide (rGO) supported magnetic core double-shell nanomaterials were successfully synthesized by an innovative four-step approach. Fe_3O_4 nanoparticles were first produced to act as cores without using any surfactants. The magnetite/silica core–shell structure was then prepared by hydrolysis of tetraethoxysilane in the presence of core particles under alkaline conditions. The outermost shell, the α-Fe_2O_3/TiO_2 layer, was grown over a magnetic core of Fe_3O_4@SiO_2 using a co-precipitation and calcination approach. Furthermore, nanohybrids were fabricated by loading Fe_3O_4@SiO_2@α-Fe_2O_3/TiO_2 nanoparticles on rGO using a hydrothermal method. Nanomaterial characterization by vibrating-sample magnetometry (VSM), X-ray photoelectron spectroscopy (XPS), and X-ray diffraction (XRD) showed both nanomaterials with and without rGO support are soft ferromagnetic and the presence of Fe_3O_4, TiO_2, Fe_2O_3 and SiO_2 in both nanomaterials. The nanohybrids exhibited increasing photocurrent as a function of illumination by cool white fluorescent light, and their magnetic property enabled the particles to be magnetically separated for recycling and reuse. The efficient photoactivity of the Fe_3O_4@SiO_2@α-Fe_2O_3/TiO_2-rGO nanohybrids was confirmed for conversion of two lignocellulose model compounds: 83.9% for conversion of D-xylose, and production of 0.49 mol lactic acid for conversion of 1 kg of sodium lignosulfonate; these results represent an improvement compared to the core double-shell nanoparticle without rGO support. Increased productivities were also obtained for four other products in conversion of sodium lignosulfonate using the rGO-supported nanomaterials compared to the ones without rGO support. These findings indicate that the rGO support improved the properties of Fe_3O_4@SiO_2@α-Fe_2O_3/TiO_2, possibly by acting as an electron acceptor—thereby avoiding high recombination of electron–hole pairs and increasing the generation of hydroxyl radicals. Our primary results suggest that the approach exemplified by the produced photocatalysts may potentially lead to cost-effective and environment-friendly strategies for reducing lignocellulosic biomass and generating value-added chemicals in large scales.

Keywords Core shell · Nanomaterials · Nanohybrids · rGO · Lignocellulose conversion · Biomass · Photocatalysis · Characterization

✉ Jia Liu
jialiu@siu.edu

[1] School of Civil, Environmental and Infrastructure Engineering, Southern Illinois University, 1230 Lincoln Dr., Carbondale, IL 62901, USA

[2] School of Chemical and Biomolecular Sciences, Southern Illinois University, 1245 Lincoln Dr., Carbondale, IL 62901, USA

[3] Artie McFerrin Department of Chemical Engineering, Texas A&M University, Jack E. Brown Chemical Engineering Building, 3122 TAMU, 100 Spence St., College Station, TX 77843, USA

[4] Materials Technology Center, Southern Illinois University, 1245 Lincoln Dr., Carbondale, IL 62901, USA

[5] College of Environmental Science and Engineering, Taiyuan University of Technology, No. 79 Yingze West Street, Taiyuan 030024, Shanxi, China

Published online: 04 May 2023

1 Introduction

Lignocellulose is the most abundant non-edible biomass feedstock; it generally originates from forestry waste, agricultural residues, municipal paper waste, and certain food waste residues [1]. Lignocellulose valorization has been studied extensively in the past twenty years [2]. However, lignocellulose is rather recalcitrant due to its highly cross-linked and complex structure, which comprises three major units: cellulose, hemicellulose, and lignin. The recalcitrant structure of lignocellulose makes the first step of depolymerization difficult and normally several processes and technologies are involved, such as gasification, pyrolytic processes assisted by strong acids or bases, hydrothermal liquefaction, and enzymatic hydrolysis [3]. However, the costs of these pretreatment processes are high, and the efficiencies are low in most cases—especially for lignin (< 10–20 wt%). In addition, the products generated under the necessarily harsh conditions may not be energetically or chemically valuable. Thus, exploring milder and cost-effective conditions is urgently needed for the valorization of lignocellulosic biomass.

Solar energy is free, abundant, and renewable. Photocatalytic processes are clean, energy-saving, and the reactions can often be performed at lower, milder temperatures by using photons instead of thermal energy. Compared to photocatalytic conversion of CO_2 into fuels and conversion of biomass into hydrogen [4, 5], photocatalytic conversion of biomass to other value-added chemicals (e.g., hydrocarbon fuels) is relatively new with comparatively fewer efforts, but a growing number of publications have begun to emerge in recent years [6] and thus interest is growing. The use of precious metal nanomaterials as catalysts (e.g., Pd, Pt, Au, Ag) for biomass photocatalytic hydrogen evolution has been studied at length [7, 8]. However, the employment of photocatalysts that do not contain precious metals and instead use earth-abundant materials is necessary for reducing the cost and making the technology easily accessible and truly sustainable. Various biomass-reforming materials have been developed with this regard, such as TiO_2-based (e.g., Ni-S/TiO_2, TiO_2/NiO), and non-TiO_2-based (e.g., ZnS-, graphitic carbon nitride (g-C_3N_4)-, and carbon-based) materials [9].

Among various semiconducting metal-oxides, TiO_2 is the most studied material as it has low or no acute toxicity, is abundant, chemically inert, and stable under UV and sunlight irradiation. Importantly, TiO_2 has already been applied to depolymerize lignin, a byproduct in the pulp and paper industry [10]. TiO_2 photocatalysis of tropical grass and rice husks can produce a wide array of soluble organic products [10]. However, TiO_2 has a large band gap of 3.2 eV and thus is only able to absorb UV light, which represents only a small fraction of solar radiation reaching the Earth's surface (i.e., ~4%). Therefore, conventional TiO_2-based photocatalysis is only cost-effective to produce high-value fine chemicals. For commodity products (with a price of a few dollars per kilogram), it is necessary to use the visible solar spectrum to make the process economical. Moreover, for photocatalytic applications, isolation of titanium oxide particles from aqueous media is essential, but it requires complex and costly processes that can lead to incomplete TiO_2 separation and cause secondary contamination [11].

One possible solution for overcoming these problems is the use of core–shell nanocomposites [12]. In a core–shell structure, the chemical composition on the surface is normally different from the core and has improved photocatalytic performance compared to each individual component, such as encapsulation of magnetic materials for magnetic separations and recycling, and activation of unique light-absorption properties [13, 14]. Magnetic core–shell structure composites have particularly gained much attention in different application fields [15]. Magnetic particles can be used as cores, and coatings of silicon oxide or titanium dioxide (or both) on these particles can be blended as shells (e.g., for catalytic properties) [16, 17]. Due to their appealing characteristics such as low toxicity, high chemical stability, high magnetic properties, and low cost, iron (II, III) oxide nanoparticles (i.e., Fe_3O_4, magnetite) are among the most promising magnetic materials [18]. Using a SiO_2 layer between Fe_3O_4 and TiO_2 helps to keep the efficiency of the core–shell photocatalyst [19]. Furthermore, coupling TiO_2 with other semiconductors can expand its response to the visible region of the electromagnetic spectrum and lower the excitons' recombination rate [11]. Hematite (α-Fe_2O_3) is a thermodynamically stable iron oxide that is non-toxic, biodegradable, and has a narrow band gap among semiconductors (i.e., 2.2 eV)[20]; moreover, its corrosion resistance and positive valence band edge position make it a potential co-material for the parent material's overall improvement [21]. The formation of α-Fe_2O_3/TiO_2 heterojunctions can boost the performance of TiO_2 photocatalysts due to the shifts of the absorption range to the visible region, faster electron transfer, and lower rate of exciton recombination [22, 23].

Supporting materials such as graphene and chemically modified graphene (e.g., graphene oxide, GO) have been hybridized with metal oxides, e.g., TiO_2, to enhance the efficiency of photocatalysis [24, 25]. Graphene, a monolayer comprised of a two-dimensional carbon atomic sheet, possesses high mobility of charge carriers, optical transparency, a huge surface area, and chemical stability [26]. Graphene can slow recombination of the photo-generated electron–hole pairs due to its excellent electron trapping and electrical conductivity properties [27]. And like α-Fe_2O_3

mentioned above, graphene can also provide a superior photo response by extending the excitation wavelength from UV into the visible region compared to bare TiO_2 [28].

In this study, a novel core double-shell structured multifunctional nanomaterial was synthesized using an improved and cost-effective method. This nanomaterial was tuned to also absorb visible light (apart from UV light), which occupies the majority of the solar emission reaching the earth's surface. The nanomaterial was also produced to have magnetic properties (specifically, superparamagnetism) for easy magnetic separation from residues after photocatalysis for reuse. The bare nanoparticle was further connected to supporting material rGO to increase photocatalytic efficiency by slowing the recombination of electron–hole pairs. The properties of the newly developed nanomaterials were characterized via various means, including scanning electron microscopy (SEM) with energy-dispersive X-ray spectroscopy (EDX), transmission electron microscopy (TEM), X-ray photoelectron spectroscopy (XPS), Brunauer–Emmett–Teller (BET) analysis, vibrating-sample magnetometry (VSM), X-ray diffraction (XRD), dynamic light scattering (DLS), UV–Vis spectroscopy, and chronoamperometry. The carbon–metal nanohybrids were utilized for the first time to transform two model lignocellulose compounds (D-xylose and sodium lignosulfonate) and the efficiencies of these processes were compared to the corresponding values obtained with bare core double-shell nanoparticles without rGO support. Considering the large quantity of photocatalysts needed in the biomass transformation process, the price of the nanomaterials is low given that these materials are abundant on earth. Moreover, their magnetic properties allow these materials to be recycled for reuse, further increasing their potential for positive environmental impact. Additionally, the experiment was conducted without the presence of oxygen since ~ 50% of the photogenerated charge carriers can be lost by reacting with oxygen [29, 30].

2 Experimental details

2.1 Synthesis of Fe_3O_4 nanoparticles

Fe_3O_4 nanoparticles were prepared according to a reported method from ferrous and ferric salts in aqueous solution without any surfactant [31]. In brief, to prepare Fe_3O_4 nanoparticles, homogeneous in size and composition, it is important to perform the reaction in an aqueous solution with a molar ratio of Fe(II)/Fe(III) of 0.5 and a pH of 11–12. Volumes of 0.85 mL of 12.1 N HCl and 25 mL of deionized and deoxygenated water (resistance of 17.8 MΩ, by bubbling nitrogen gas for 30 min) were mixed, then 8.65 g of $FeCl_3{\cdot}6H_2O$ and 3.17 g of $FeCl_2{\cdot}4H_2O$ were successively dissolved in the solution under vigorous stirring under nitrogen environment. The resulting solution was added dropwise under nitrogen environment into 250 mL of 2.5 N NH_4OH solution under vigorous stirring. The last step generated an instant black precipitate. The paramagnetism was checked in situ by placing a magnet near the black precipitate. Afterwards, the precipitate was isolated by the magnetic field and the supernatant was decanted. Deionized and deoxygenated water was added to the precipitate and the solution was decanted after centrifugation at 4000 rpm (radius 110 mm). After repeating the last step for three times, 500 mL of 0.01 M HCl solution was added to the precipitate with stirring to neutralize the anionic charges on the nanoparticles and form the cationic colloidal nanoparticles. The pH of the suspension was adjusted to 7.0 using HCl and NaOH. The suspension was freeze dried to isolate the nanoparticles.

2.2 Synthesis of Fe_3O_4@SiO_2 core–shell nanoparticles

Inner shell SiO_2 was prepared by a sol–gel process using the most prevalent alkoxide of silicon as the precursor. At first, a mixture of 120 mL deoxygenated water, 250 mL ethanol, and 6 mL ammonia solution (25%) was prepared. Magnetite Fe_3O_4 nanoparticle of 0.88 g was dispersed into this solution and sonicated. Then the mixture was kept at 45 °C in water bath. A solution of 50 mL ethanol containing 4 mL of tetraethyl orthosilicate (TEOS) was separately prepared and added slowly to the magnetite mixture at 45 °C. The resulting mixture was mechanically stirred at 45 °C for 8 h with a stirring speed of 120 rpm (radius 6.5 mm) for hydrolysis and condensation reactions of TEOS in ethanol. Condensation was not limited and continued indefinitely until there was precipitation of SiO_2 on Fe_3O_4. Finally, the product was separated in a magnetic field and rinsed repeatedly with ethanol. The samples were dried under nitrogen flow. The core shell structured nanoparticle Fe_3O_4@SiO_2 was thus obtained.

2.3 Synthesis of Fe_3O_4@SiO_2@α-Fe_2O_3/TiO_2 core double-shell nanoparticles

A suspension of 0.3 g of Fe_3O_4@SiO_2 with 100 mL deoxygenated water was made and sonicated for 20 min. Then, 1.0 g of $FeCl_3{\cdot}6H_2O$ and 0.83 g of $FeCl_2{\cdot}4H_2O$ were successively dissolved in the core–shell dispersion. The solution was kept in the dark and stirred for about 5 min. Then 470 µL of $TiCl_3$ solution (~ 20% w/v in 2 N hydrochloric acid) was added into this solution. The mixture was stirred vigorously and NH_4OH solution (25%) was added dropwise into the solution using a syringe pump. The pH of the solution was measured continuously after adding the NH_4OH solution and the addition was immediately stopped as soon as the pH reached 9.0. The mixture was then diluted to 200 mL

using deionized water and placed in a strong magnetic field to separate the particles from the solution. The particles were washed with deionized water for 3 to 5 times and then dried at 50 ºC for 12 h. After crushing, calcination of the dried particles under nitrogen atmosphere at 400 ºC was performed for 1 h. Crystallized anatase was obtained in this way. These powders were then calcined under oxygen atmosphere at 450 ºC for 2 h and the final obtained core-double shell products were stored in a desiccator.

2.4 Synthesis of reduced GO (rGO) supported core-double shell nanoparticles

rGO-loaded core-double shell nanoparticles (Fe_3O_4@SiO_2@α-Fe_2O_3/TiO_2-rGO) were prepared using a hydrothermal method. GO (99.3%) was purchased from US Research Nanomaterials, Inc. First, the GO (0.157 g) was suspended in a liquid made by 50 mL of deionized water and 50 mL of ethanol, and sonicated for 15 min. After that, the core-double shell nanoparticles (0.2355 g) were added into this GO suspension. The ratio of GO and Fe_3O_4@SiO_2@α-Fe_2O_3/TiO_2 was controlled to be 2:3 (w/w). This ratio was determined by referring to the information from literature on the ratio of Fe_3O_4 to GO when preparing Fe_3O_4–GO nanohybrid [32, 33], and preliminary tests in the lab, to ensure the nanohybrids have proper magnetic and photocatalytic properties. The reduction of GO and the loading of the nanoparticles on the reduced GO sheets were achieved simultaneously after stirring the mixture for 2 h and transferring the solution to a 200 mL Teflon-lined stainless-steel autoclave for 3 h at 120 ºC. The resulting composite was recovered by centrifugation at 4,000 rpm (radius 110 mm) for 15 min, rinsed with ultrapure water with the help of its magnetic property, and fully dried at 60 ºC overnight. Finally, the material was grinded in a mortar with a pestle and black powder was formed which was the rGO supported core-double shell nanoparticles.

2.5 Nanomaterial characterization

The produced nanoparticles were characterized by scanning electron microscopy (SEM, FEI Quanta FEG 450) with an EDX detector, and transmission electron microscopy (Hitachi H 7650), for their morphology and structural characteristics. The nanoparticles were sonicated for at least 15 min in acetone, then a suspension of 10 µL was dispersed onto a piece of carbon tape, dried, and Au-sputter coated to enhance SEM image quality. TEM imaging was operated at 60 kV acceleration voltages, with direct magnification of 40,000×. Prior to TEM analysis, the nanoparticles were dispersed in ethanol using an ultrasonic bath. Subsequently, a drop of the dispersion was applied to a holey carbon film and dried in an oven at 60 °C for 10 to 15 min for TEM observation. Size distribution of the nanoparticles was analyzed by dynamic light scattering according to our previous method (DLS, DynaPro NanoStar, Wyatt Technology, Santa Barbara, CA, USA) [34–36]. Absorption spectra of the nanoparticles were obtained by using a UV–Vis spectrophotometer (ThermoFisher Scientific BioMate™ 3S) scanned in the range of 190–800 nm. Tauc plots were made from the absorption spectra to determine the optical bandgaps of the nanomaterials. Specific surface area of the nanomaterials was determined by using a Quantachrome Autosorb-iQ3-MP/Kr BET Surface Analyzer. The nanomaterials were also characterized using a Kratos Axis Supra x-ray photoelectron spectrometer (XPS). The XPS can obtain information on the chemical and electronic state of a sample's elemental components to a penetration depth of ~ 10 nm. Hysteresis loop was measured by a Quantum Design MPMS3 SQUID Magnetometer. Scanning for the core double-shell nanomaterials with and without rGO support was performed in an ethanol solution. In addition, the nanomaterials were analyzed with a Rigaku Ultima IV X-ray diffractometer (XRD) using Cu K_α radiation at a 0.02° 2θ step from 5–90° 2θ.

2.6 Photocurrent measurement of the nanomaterials

A Gamry Reference 3000 Potentiostat was used to measure the photocurrent responses of all the nanoparticles with and without fluorescent light illumination provided by a photoreactor (Luzchem Research Inc., LZC-4 V, Canada). The fluorescent light used is ideal for emulation of office light. It has a majority of 92% visible light energy, with the rest being 3% UVA, < 1% UVB, < 1% UVC, and 5% NIR. The responses were recorded by chronoamperometry scans for different nanomaterials. Before the experiment, the surface of graphite rods was coated with nanomaterials with or without rGO support (0.15 g) using 5 mL of Nafion solution (5% w/w in water and 1-propanol). Photocurrent collection from the nanomaterial coated graphite rod as counter electrode was performed in a three-electrode cell with a platinum (Pt) rod working electrode and an Ag/AgCl reference electrode. The nanomaterial coated graphite rods were illuminated under N_2 gas saturation, using methyl viologen (1 mM), KNO_3 (5 mM), and CH_3OH (10% v/v) as electron shuttle, electrolyte, and hole scavenger, respectively. A bias voltage of 150 mV was set during the scan.

2.7 Photocatalytic conversion of model compounds and HPLC analysis

Nitrogen dried nanoparticles of 25 mg were added to 20 mL deionized water and sonicated for 20 min to properly disperse the nanoparticles in an aqueous suspension. D-xylose was used as a model compound of hemicellulose

after its decomposition [37]. Sodium lignosulfonate ($C_{20}H_{24}Na_2O_{10}S_2$) was used as a lignin model compound [38]. In each of the sample vials with air-tight caps, 8 mL of deionized water was added under N_2 environment, and D-xylose or sodium lignosulfonate was also added to make a 17 g/L solution under N_2 environment, and photocatalyzed under fluorescent light using core-double shell nanoparticles with and without rGO support. Different nanoparticle suspensions of 2 mL were added into each vial making the final concentration of the nanoparticles equal to 250 mg/L. After that, the vials were wrapped up, the rubber caps were sealed to the vials using aluminum seals, and the vials were shaken well. To create an environment without presence of oxygen, one needle injecting nitrogen and another needle releasing air from the vial were placed into the rubber cap to purge the samples off oxygen before the photoreaction. The small holes were then sealed using silicone and the samples were placed in a photoreactor (Luzchem, LZC-4X) equipped with 14 LZC-VIS light bulbs. A visible light intensity of 4.62 mW/cm^2 was provided. During a reaction time of 4 h, samples were taken at certain time intervals and prepared for HPLC analysis. Each sample was first passed through a 0.22 µm polytetrafluoroethylene (PTFE) membrane filter (GE Healthcare Whatman™) and then run through the HPLC equipped with a refractive index detector and an Aminex HPX-87 column (5 µm, 30 cm × 4.6 mm, Bio-Rad, CA, USA). The temperature of the column was set at 35 °C. Sulfuric acid of a concentration of 5 mmol/L was used as the mobile phase with a flow rate of 0.6 mL/min. After 4 h of reaction, the nanomaterials in each vial were collected by an external magnetic field (using a 24″ tube neodymium magnet with holding force of 6.1 lbs, Bunting Magnetics Co.), centrifuged at 4000 g, and air dried at 40 °C for EDX analysis.

2.8 Determination of the concentrations of hydroxyl radicals

Terephthalic acid (TPA, 0.5 mM in 2 mM NaOH solution) was employed as the probe molecule to determine the amount of hydroxyl radicals ·OH generated in the biomass conversion process. The detailed method for ·OH detection was reported in our previous studies [39, 40]. In breif, 1 mL of TPA stock solution was added to the vial filled with 250 mg/L of nanomaterials with or without the rGO support. The vial was exposed to fluorescent light. At different time intervals, samples were filtered by 0.22 µm syringe filter, and measured using a Shimadzu Prominence UPLC system (Shimadzu Co. Ltd, Japan) connected to a fluorescence detector RF-10A XL (Shimadzu, Japan).

3 Results and discussion

3.1 Nanoparticle characterization

The TEM images of Fe_3O_4 nanoparticles prepared with NH_4OH as a precipitating agent showed that the sizes of individual particles were comparable and in the range of 10–15 nm (Fig. 1a). Some aggregations of the Fe_3O_4 nanoparticles were likely due to the magnetostatic interactions of these particles (Fig. 1a). At first, NaOH was used as the precipitant as described in the literature [31, 41]. However, NaOH is a strong base that gives rise to a high concentration of hydroxide ions quickly, which is favorable for nanoparticle growth. Consequently, the growth of the nanoparticles was faster than the nucleation step and the particle size increased rapidly. Therefore, the Fe_3O_4 nanoparticles used in this work were instead created using a weak base (NH_4OH) as the precipitating agent, which resulted in a significant reduction in the size of the fabricated particles.

The TEM images of $Fe_3O_4@SiO_2$ (core–shell nanoparticles) and $Fe_3O_4@SiO_2@\alpha\text{-}Fe_2O_3/TiO_2$ (bare core double-shell nanoparticles) indicated the size of the particles increased gradually with each layer of the coating (Fig. 1b,c). The core–shell structure of $Fe_3O_4@SiO_2$ can be seen in the image (Fig. 1b). These particles were aggregated partly due to their magnetic properties. The core–shell structure of $Fe_3O_4@SiO_2@\alpha\text{-}Fe_2O_3/TiO_2$ can also be seen in Fig. 1c,d; however, the double-shell structure was not clearly manifested in the images, likely due to the relatively low resolutions of the images and the aggregation of the particles. In this designed core double-shell structure of $Fe_3O_4@SiO_2@\alpha\text{-}Fe_2O_3/TiO_2$, the SiO_2 middle layer is crucial for retention of both the superparamagnetic properties of the inner Fe_3O_4 component and the photocatalytic properties of the external $\alpha\text{-}Fe_2O_3/TiO_2$ layer. The wide bandgap of the SiO_2 (7.52—9.60 eV [42]) electronic barrier prevents direct contact and electron injection from $\alpha\text{-}Fe_2O_3/TiO_2$ to Fe_3O_4, avoiding charge recombination at the interface. Moreover, a SiO_2 middle layer is an excellent adsorbent for organic molecules, increasing their enrichment around the titania-iron oxide photoactive layer and thus enhancing the photocatalytic performance. Wrinkled regions and scrolled edges of the graphene sheets can be observed in the TEM images of rGO-loaded core double-shell nanoparticles (Fig. 1d). The core double-shell nanoparticles were distributed but partially agglomerated on the surface of the rGO sheets, reflecting the sequence of loading rGO as the support material to the core double-shell nanoparticles in the last step (Fig. 1d).

The images of Fe_3O_4 core, $Fe_3O_4@SiO_2$ core shell, $Fe_3O_4@SiO_2@\alpha\text{-}Fe_2O_3/TiO_2$ core double-shell, and rGO loaded core-double shell nanoparticles were shown in

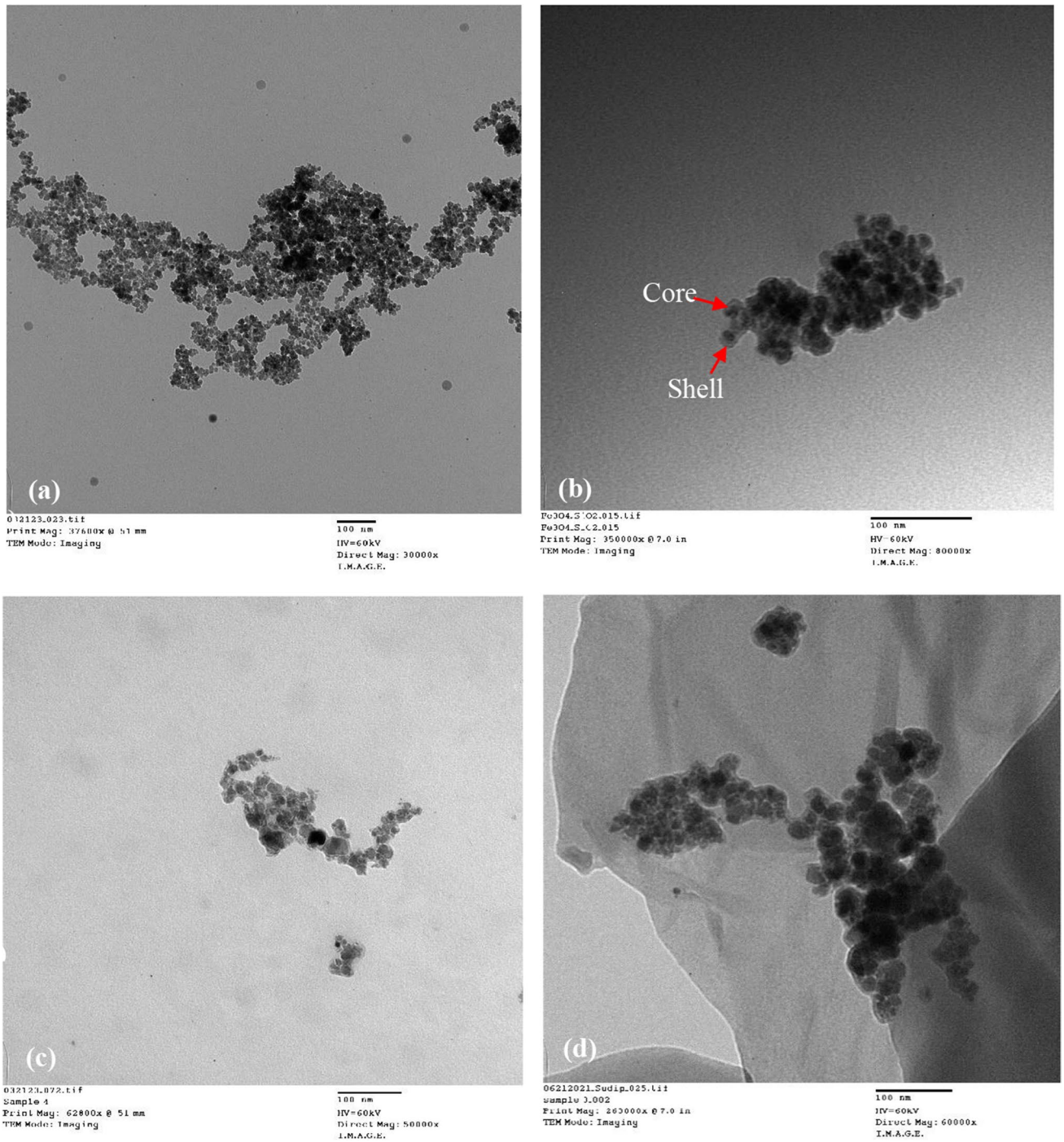

Fig. 1 TEM images of (**a**) Fe_3O_4, (**b**) $Fe_3O_4@SiO_2$, (**c**) $Fe_3O_4@SiO_2@\alpha\text{-}Fe_2O_3/TiO_2$ core double-shell nanoparticles, and (**d**) rGO loaded core-double shell nanoparticles

Fig. S1. The DLS result of $Fe_3O_4@SiO_2@\alpha\text{-}Fe_2O_3/TiO_2$ core double-shell nanoparticles showed that 33.92% of the nanoparticles were within 100 nm in size (Fig. S2a). This was likely due to the fact that the magnetite nanoparticles were unstable in water and were prone to agglomerate owing to their high specific surface area and magnetization. For rGO-supported core double-shell nanoparticles, 16.32% of the nanoparticles were within 100 nm of their hydrodynamic diameter (Fig. S2b). These results revealed that supporting the zero-dimensional core double-shell nanoparticles by the two-dimensional material placed some effect to increase the overall size of the nanoparticles.

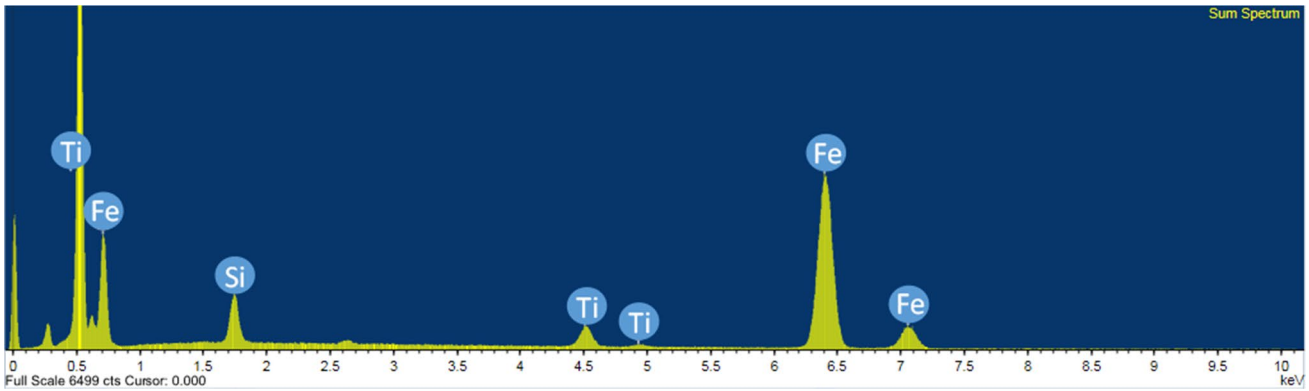

Fig. 2 EDX pattern of Fe_3O_4@SiO_2@α-Fe_2O_3/TiO_2 core double-shell nanoparticles fabricated in this study

The elemental composition of Fe_3O_4@SiO_2@α-Fe_2O_3/TiO_2 was determined by energy dispersive X-ray (EDX) analysis. The EDX analysis confirmed the presence of titanium, silicon, and iron elements in the core double-shell nanoparticles (Fig. 2). From the EDX analysis, the atomic percentages of constituent elements Ti, Si, and Fe are 5.26%, 14.37%, and 80.37%, respectively, in the nanoparticles. The weight percentages of the constituent elements Ti, Si, and Fe are 7.85%, 4.90%, and 87.25%, respectively. This result was slightly different from the weight percentages of the Ti, Si, and Fe elements used in the fabrication of the nanoparticles that composed all three layers of the core double-shell nanoparticles, i.e., 11.86%, 4.03%, and 84.11%, respectively. Thus, successful synthesis of the nanomaterial composed of the three elements was demonstrated, although it was likely that a low percentage of the Fe_3O_4@SiO_2 core–shell was not properly coated by the next layer of the material, since the weight fraction of Ti – the element in the outer layer – was lower in the fabricated nanoparticles compared to that used in the synthesis of the nanoparticles.

The UV–visible absorption spectrum and the Tauc plot of the bare core double-shell nanoparticles are shown in Fig. 3a. It can be seen that the nanoparticles exhibit wide absorption from ~ 250 nm to ~ 700 nm, and the absorption value in the visible-light range was particularly high. The region showing a steep, linear increase of light absorption with increasing photon energy is characteristic of semiconductor materials [43]. The *x*-axis intersection point of the linear fit of the Tauc plot gives an estimate of the band gap energy [43]. Therefore, the direct band gap energy calculated for the core double-shell nanoparticles was found to be 2.814 eV (Fig. 3a). Similarly, the absorption spectrum and Tauc plot were drawn using the data from a UV–Vis spectrophotometer for rGO-supported core

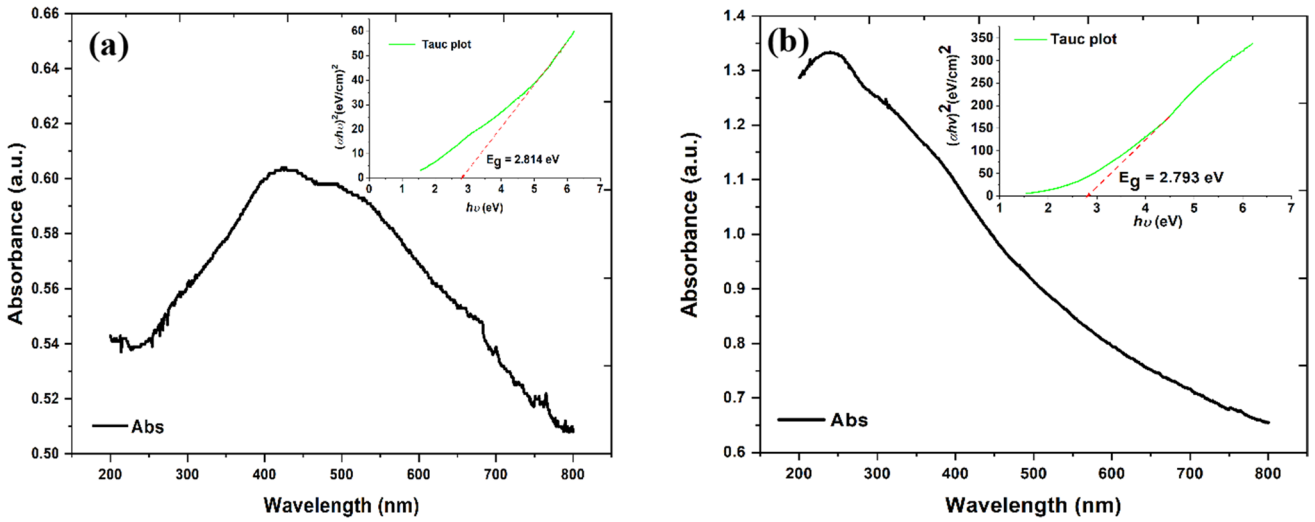

Fig. 3 Absorption spectra and Tauc plots for (**a**) bare core double-shell nanoparticles, and (**b**) rGO supported core double-shell nanoparticles. Concentration of the nanoparticles is 250 mg/L

double-shell nanoparticles (Fig. 3b). It was found that the rGO supported nanoparticles had wider and higher absorption from 200 to 700 nm compared to bare core double-shell nanoparticles, with a slightly lower band gap energy of 2.793 eV (Fig. 3b). These band gap values revealed responses of these two types of nanoparticles under visible light. The shift of the peak for rGO-supported nanomaterials compared to the bare nanomaterials reflected fabrication of rGO (having a peak at ~ 260 nm [44]) to the nanohybrids.

The specific surface area determined by BET analysis is 148.692 m^2/g for $Fe_3O_4@SiO_2@\alpha\text{-}Fe_2O_3/TiO_2$, which is comparable to the specific surface area of 146.574 m^2/g for $Fe_3O_4@SiO_2@\alpha\text{-}Fe_2O_3/TiO_2$-rGO. XPS results of the synthesized nanomaterials are shown in Fig. 4 and Table 1. From the results, Fe_2O_3 and TiO_2 were identified in both

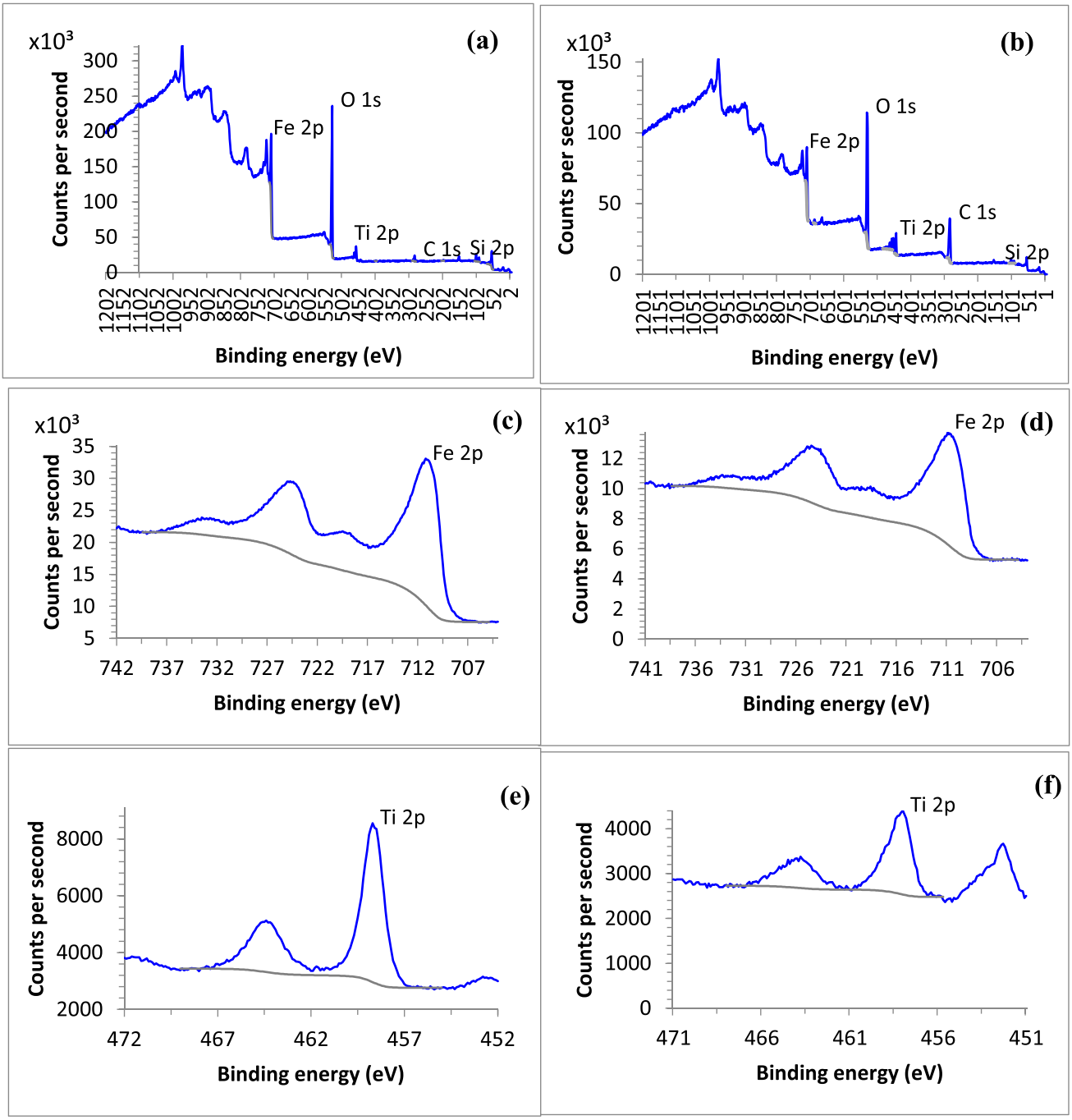

Fig. 4 XPS spectra of $Fe_3O_4@SiO_2@\alpha\text{-}Fe_2O_3/TiO_2$ (**a**,**c**,**e**,**g**,**i**,**k**) and $Fe_3O_4@SiO_2@\alpha\text{-}Fe_2O_3/TiO_2$-rGO (**b**,**d**,**f**,**h**,**j**,**l**). (a,b) survey, (c,d) Fe 2p, (e,f) Ti 2p, (g,h) Si 2p, (i,j) O 1 s, (k,l) C 1 s, (m,n) In 3d. Indium (In) was used as the internal standard

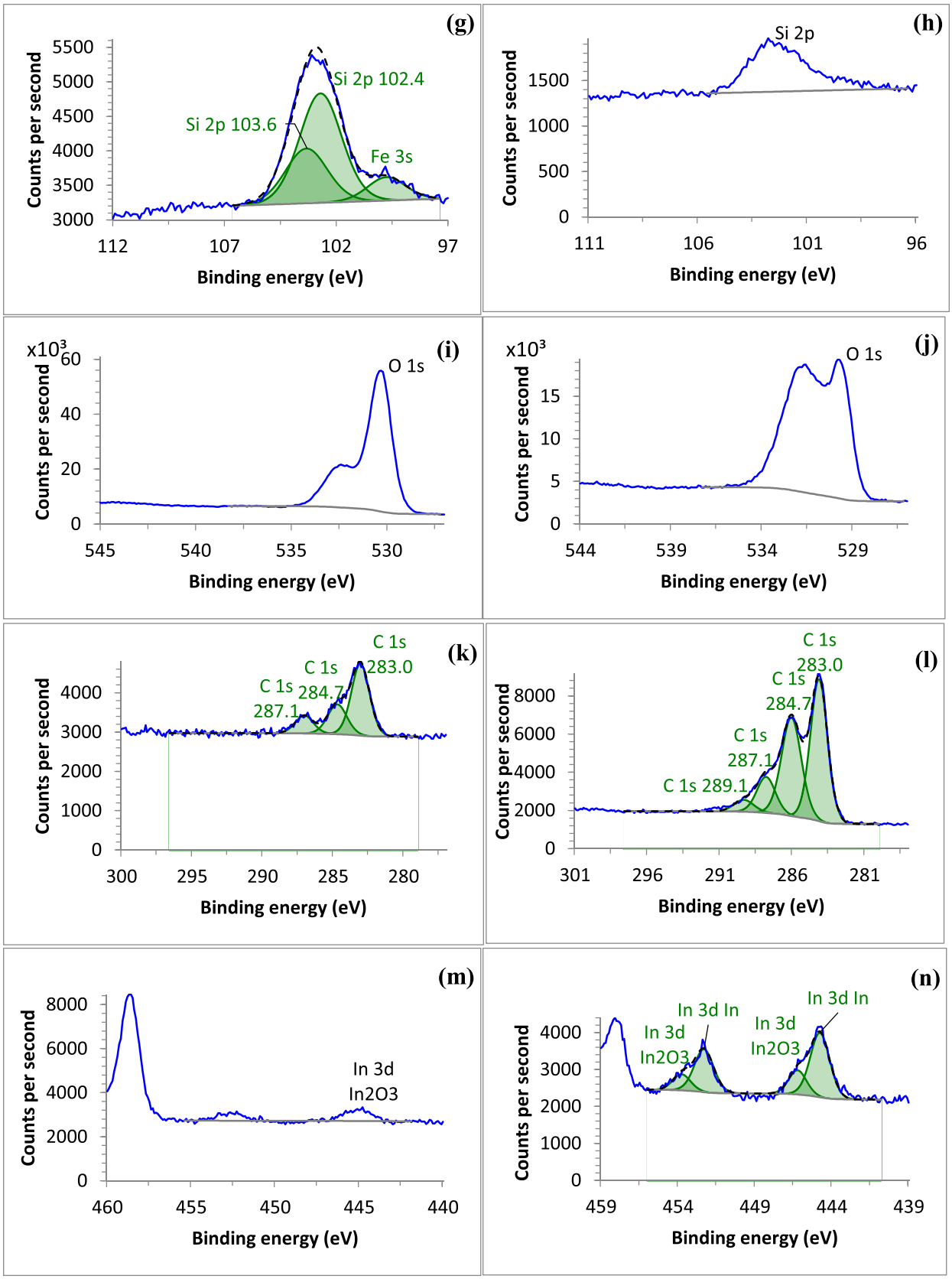

Fig. 4 (continued)

Table 1 XPS quantification for (a) Fe_3O_4@SiO_2@α-Fe_2O_3/TiO_2 and (b) Fe_3O_4@SiO_2@α-Fe_2O_3/TiO_2-rGO nanomaterials

(a) Name	Atomic conc. [%]	Error [%]
In 3d In_2O_3	0.11	0.02
Si 2p 102.4	4.86	0.31
Si 2p 103.6	2.43	0.33
Ti 2p	2.58	0.02
O 1 s	54.75	0.30
Fe 2p	27.78	0.16
C 1 s	7.49	0.22
(b) Name	Atomic conc. [%]	Error [%]
In 3d In	0.32	0.03
In 3d In_2O_3	0.11	0.02
Si 2p	2.96	0.12
Ti 2p	1.22	0.02
O 1 s	39.99	0.14
Fe 2p	11.81	0.07
C 1 s	43.61	0.16

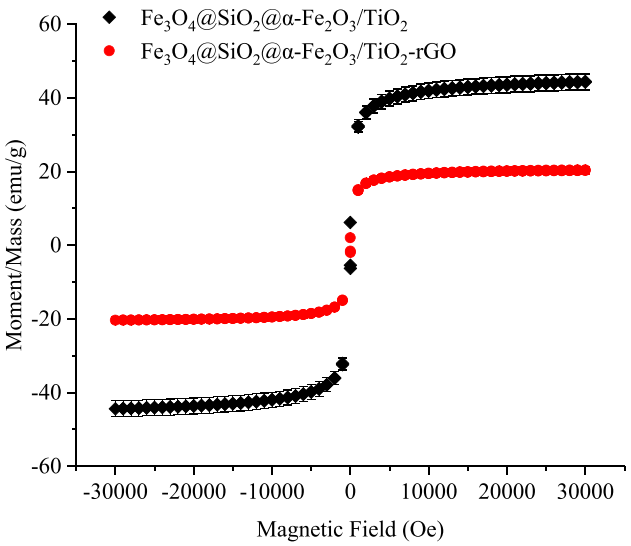

Fig. 5 Magnetic hysteresis loops of Fe_3O_4@SiO_2@α-Fe_2O_3/TiO_2 and Fe_3O_4@SiO_2@α-Fe_2O_3/TiO_2-rGO nanomaterials

nanomaterials with and without rGO support (Fig. 4c-f). The presence of SiO_2 can also be detected in both types of nanomaterials (Fig. 4g-h). The ratio of Fe:Ti:Si in the nanomaterials without rGO support is 10.8:1:2.8, which is comparable to the ratio of Fe:Ti:Si in the nanomaterials with rGO support of 9.7:1:2.4. With rGO support, the ratio of C:Fe is significantly increased in the nanomaterials compared to those without rGO support (Table 1). It is worthy to note that because of the surface sensitivity of XPS, carbon can be detected in materials (e.g., once exposed to the atmosphere, typically with a layer thickness of 1–2 nm) even when no carbon was added in preparing the materials. XRD results revealed the presence of magnetite (Fe_3O_4) in both nanomaterials with and without rGO support, however, the SiO_2 and α-Fe_2O_3/TiO_2 double shells constructed the nanomaterials were likely very thin (Fig. S3), which is in accordance with the TEM observations.

The hysteresis loop of the mass normalized magnetization versus the magnetic field is plotted in Fig. 5. Overall, the two nanomaterials with and without rGO support both show the behavior of a soft ferromagnet with no measurable coercive field (that is as expected for a liquid suspension). The saturated moment for the core double-shell nanomaterials without rGO support is significantly larger than that of the core double-shell nanomaterials with rGO support (Fig. 5).

3.2 Photocurrent responses of the nanoparticles

The photocurrent response of the core double-shell nanoparticles coated as a thin layer on graphite rod electrodes under alternating light-on / light-off conditions showed that the photocurrent increased every time on the electrode that was illuminated (Fig. S4a); correspondingly, when the light was turned off, the current decreased (Fig. S4a). A similar result was obtained when the photocurrent response of the rGO-supported core double-shell nanoparticles was tested using chronoamperometry scan under alternating light-on / light-off conditions (Fig. S4b). Since photocurrent is determined as the difference between current under light and dark conditions, the measured results indicated photocurrent was successfully generated using both types of fabricated nanomaterials.

3.3 Conversion of biomass model compounds by the fabricated nanomaterials under light

The nanomaterials produced in this study were successfully tested for their photocatalytic efficiencies under cool white fluorescent light for the conversion of a hemicellulose model compound and a lignin model compound. The conversion efficiencies of D-xylose were 62.2% and 80.0% using the bare nanoparticles after 2 and 4 h, respectively (Fig. 6). The efficiencies were further enhanced to 63.5% and 83.9% using the rGO-supported nanoparticles after 2 and 4 h, respectively (Fig. 6). No transformation product from D-xylose was detected in this study using the analytic method in HPLC. In the literature, selective oxidation of D-xylose into D-xylonic acid was reported using an N-doped defect-rich carbon as a metal-free catalyst in alkaline aqueous solution at 100 °C [45]; in comparison, photocatalytic reduction of D-xylose to xylitol over Cu-doped ZnO was reported under UVA light illumination [46]. Our study reached higher conversion efficiency in a shorter time compared to the 33.7% conversion achieved after 7 h using the Cu-doped ZnO nanoparticle

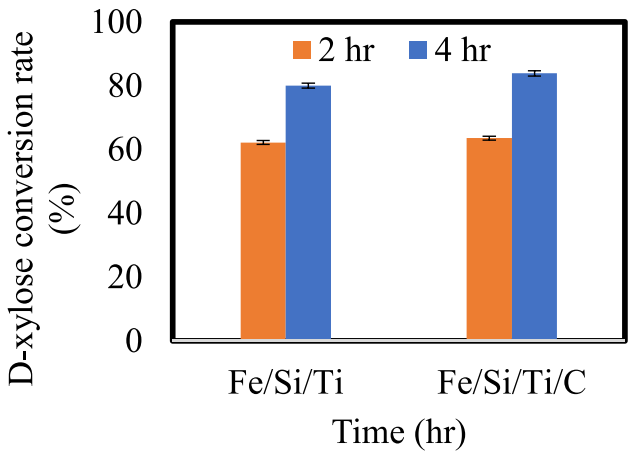

Fig. 6 Conversion efficiency of D-xylose in absence of oxygen under fluorescent light using core double-shell nanoparticles with and without rGO support. D-xylose = 17 g/L, nanoparticle = 250 mg/L, light intensity = 4.62 mW/cm^2. Fe/Si/Ti is an abbreviation of Fe_3O_4@SiO_2@α-Fe_2O_3/TiO_2; Fe/Si/Ti/C is an abbreviation of Fe_3O_4@SiO_2@α-Fe_2O_3/TiO_2-rGO

photocatalysts; thus, the catalysts developed in this study possess enhanced photocatalytic properties.

Both nanomaterials with and without rGO support were recycled by taking advantage of their magnetic properties after conversion of D-xylose and characterized using EDX. The results showed that the atomic percentages of carbon were significantly increased for the nanomaterials with rGO support (Table 2). Furthermore, the atomic percentages of carbon were significantly increased after the reaction for both nanomaterials with and without rGO support (Table 2), which indicated likely adsorption of D-xylose and molecules formed in the transformation process to the nanomaterials. It is worthy to note that when using EDX, the detected percentage of carbon in a nanomaterial is higher than the real percentage, this is because carbon tape is used for sample preparation for EDX analysis. More information on EDX mapping analysis of Fe_3O_4@SiO_2@α-Fe_2O_3/TiO_2 and Fe_3O_4@SiO_2@α-Fe_2O_3/TiO_2-rGO nanomaterials before and after conversion of D-xylose under fluorescent light was reported in the Supporting Information (Fig. S5&S6).

Table 2 Atomic percentages of elements determined by EDX analysis in (a) Fe_3O_4@SiO_2@α-Fe_2O_3/TiO_2 and (b) Fe_3O_4@SiO_2@α-Fe_2O_3/TiO_2-rGO nanomaterials before and after conversion of D-xylose under fluorescent light

(a) Element	Before reaction		After reaction	
	Atomic %	S.D	Atomic %	S.D
C	10.67	2.03	22.61	0.68
O	56.99	1.90	55.98	2.77
Si	2.41	0.13	1.58	0.10
Ti	2.03	0.26	1.42	0.09
Fe	27.90	3.61	18.42	2.13
(b) Element	Before reaction		After reaction	
	Atomic %	S.D	Atomic %	S.D
C	41.94	10.96	58.84	5.13
O	44.15	7.53	37.83	3.94
Si	1.15	0.59	0.33	0.11
Ti	0.93	0.24	0.22	0.14
Fe	11.84	2.66	2.78	1.42

Figure 7 shows the photocatalytic conversion of sodium lignosulfonate using core double-shell nanoparticles and rGO-supported core double-shell nanoparticles to valuable products. Different products including lactic acid, acetic acid, formic acid, xylose, and arabinose were obtained in the absence of oxygen under sample illumination. Lactic acid, acetic acid, and formic acid are building blocks that can be converted to useful derivatives or secondary chemicals for various products and applications [47]. Moreover, xylose and arabinose can be transformed to produce such building blocks using available commercial processes that have very few technical barriers [47]. As another building block, xylitol can be obtained by the reduction of xylose [48], whereas xylonic acid can be obtained by the oxidation of xylose [49]; similarly, arabinitol can be formed by the reduction of arabinose [50]. Considering the low cost of the raw materials, the mild reaction conditions under cool white fluorescent light, and the recyclability of the photocatalysts (Fig. S7), the method developed herein can potentially overcome the economic hurdles of large capital investments—and thus can potentially allow the facile creation of molecular building blocks in ways that compete with approaches wherein similar compounds are created with existing (but perhaps less-green) methods with low market price.

In the literature, oxidative treatment of lignin (e.g., via ozone at ambient conditions, or using other oxidizers (e.g., air, pure oxygen, or hydrogen peroxide) under high temperatures (150–250 °C) and pressures (10–20 bar)) converts it to carboxylic acids, carbon dioxide, and water [51]. In a biochemical system, lignin valorization is achieved through depolymerization and funneling various lignin-derived aromatics into protocatechuate and catechol. The central intermediates are then converted to value-added compounds via aromatic ring cleavage and the TCA cycle. The TCA cycle uses the molecules (e.g., succinate, acetyl-CoA, and pyruvate) produced from aromatic ring cleavage that enter the cycle for cell growth and product synthesis [52]. Furthermore, cleavage of the aromatic carbon skeleton and rearrangement of benzene by a trinuclear titanium polyhydride complex was reported [53]. In our study, the destruction of aromatic components of sodium lignosulfonate was achieved using the core double-shell nanoparticles both with and without rGO under light, likely due to complex processes involving reactive oxygen species and/or reactive photoelectrons [54] (Fig. 8). In photocatalytic oxidation of

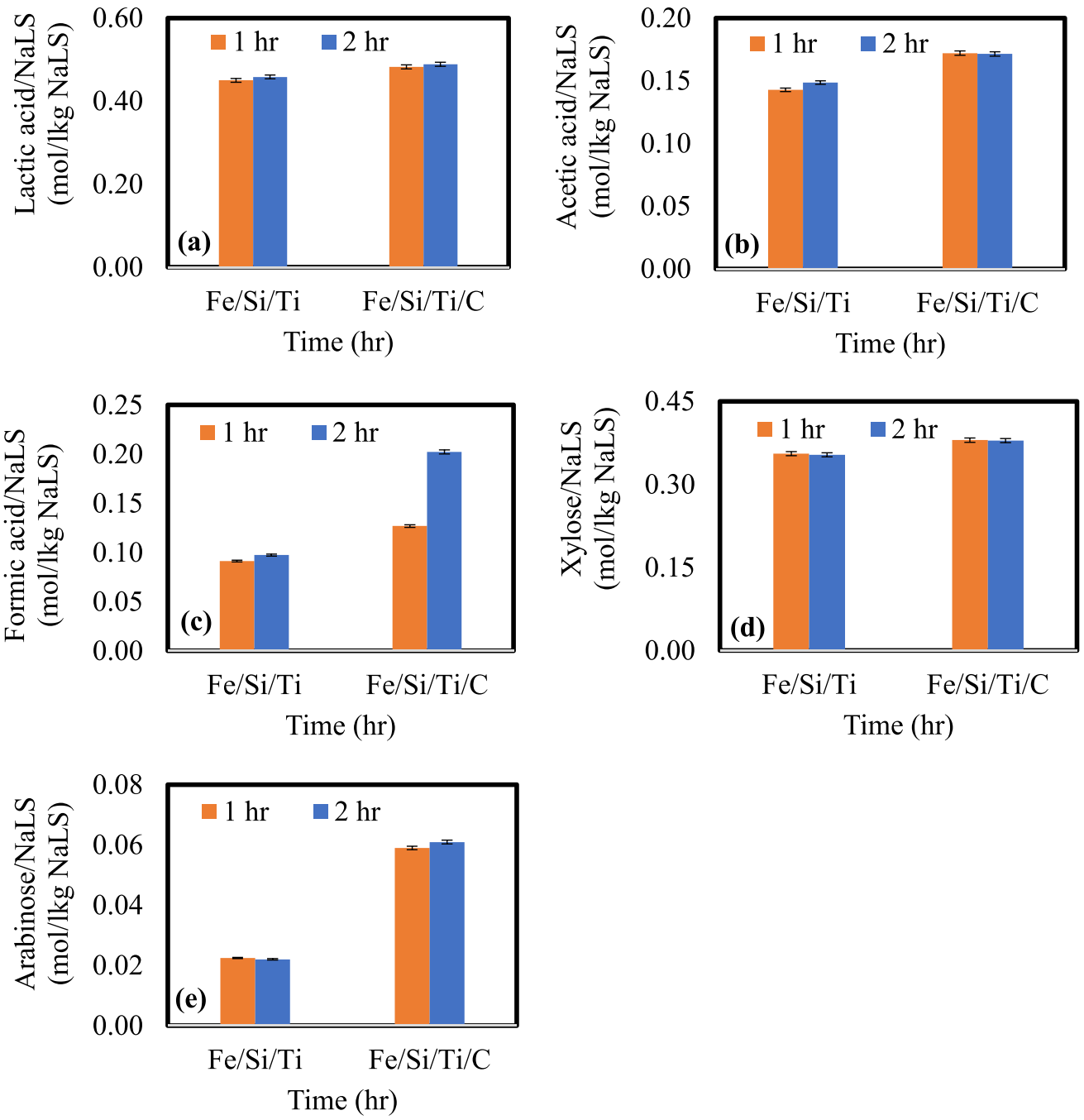

Fig. 7 Yield of main products obtained from sodium lignosulfonate (NaSL) in the absence of oxygen under fluorescent light using core double-shell nanoparticles with and without rGO support. NaSL = 17 g/L, nanoparticle = 250 mg/L, light intensity = 4.62 mW/cm^2. Fe/Si/Ti is an abbreviation of Fe_3O_4@SiO_2@α-Fe_2O_3/TiO_2; Fe/Si/Ti/C is an abbreviation of Fe_3O_4@SiO_2@α-Fe_2O_3/TiO_2-rGO

lignin, lignin depolymerization can be achieved using the photogenerated hydroxyl radicals ·OH [55]. In photocatalytic reduction of lignin, photoelectrons generated from the heterogeneous photocatalysts can promote C–O/C–C bond cleavage [54].

In addition to the detected compounds, an unidentified product (with retention time of 11.209 min) was detected when using rGO-loaded nanomaterials, the area of the product increased with time over 3 h of the reaction. It is likely for this undetected compound to be a sugar or acid given the range of the retention time. Their area percentages in comparison to those of other products in the chromatograms were very low, which indicated low concentrations; thus, this undetected compound was comparatively insignificant. As

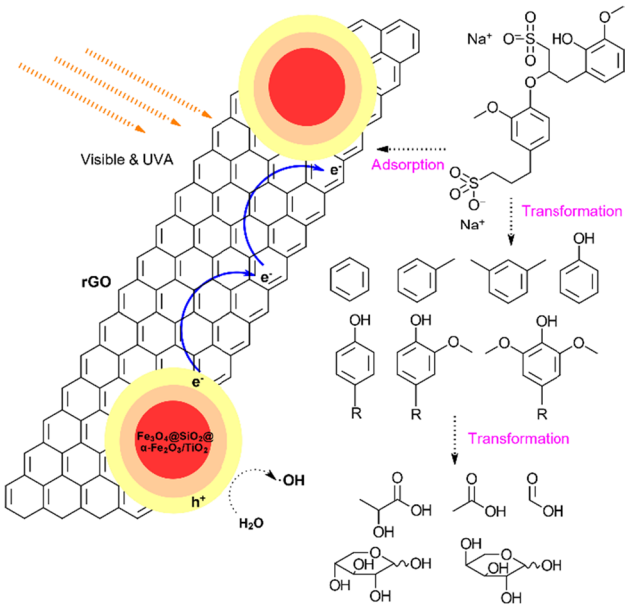

Fig. 8 Proposed transformation of sodium lignosulfonate using Fe_3O_4@SiO_2@α-Fe_2O_3/TiO_2-rGO under fluorescent light. The proposed aromatic intermediates include benzene, toluene, xylene, phenol, and complex aromatics

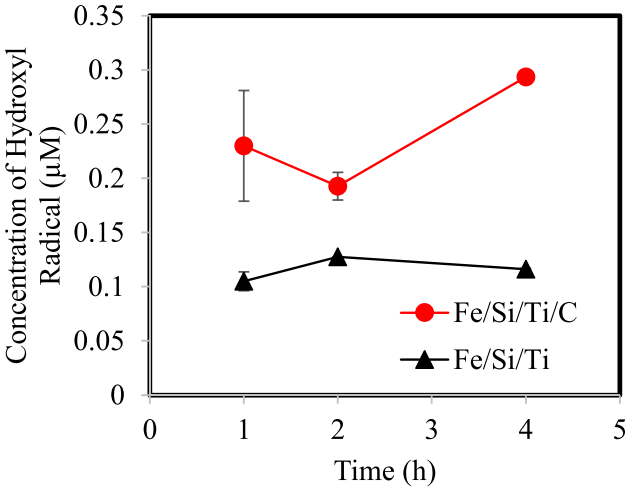

Fig. 9 Concentrations of photogenerated hydroxyl radicals ·OH using core double-shell nanoparticles with and without rGO support under fluorescent light. Fe/Si/Ti is an abbreviation of Fe_3O_4@SiO_2@α-Fe_2O_3/TiO_2; Fe/Si/Ti/C is an abbreviation of Fe_3O_4@SiO_2@α-Fe_2O_3/TiO_2-rGO

seen in Fig. 7, most of the concentrations of these products were only slightly increased using a given type of nanomaterial when the photoreaction time was increased from 1 to 2 h, which may be too short to see significant increases in the product concentrations. For each product, higher concentrations were obtained when using rGO-loaded nanoparticles as compared to the bare nanoparticles (Fig. 7). For example, production of 0.49 mol-lactic acid/kg-sodium lignosulfonate was achieved using rGO-supported nanoparticles, an improvement compared to the bare nanoparticle (which yielded production of 0.46 mol-lactic acid/kg-sodium lignosulfonate, Fig. 7). The yield of some compounds (e.g., xylose) was low, perhaps because the product was converted to carbon dioxide and water soon after its generation. Indeed, high concentrations of carbonates were detected by HPLC using both types of nanomaterials studied here. In the literature, a value-added product, vanillin, was obtained from photocatalytic conversion of sodium lignosulfonate using mesoporous TiO_2 (derived from facile calcination of MIL-125) under illumination by xenon lamp; however, the yield was low, 0.014 mol-vanillin/kg-sodium lignosulfonate [53]. In another study, phenol was obtained from conversion of sodium lignosulfonate using nitrogen-doped iron titanate films under both simulated solar and visible light, with the phenol yields of 0.96 μg/mL and 1.20 μg/mL, respectively [56]. During lignin processing, low-molecular weight products (C1-C3, etc.) can also be produced along with aromatics. These light products may include formic or acetic acids as well as aliphatics and olefins [57]. Thus, although aromatic chemicals were not detected by the method used, the confirmed products in this study showed lignin conversion to value-added products. Additionally, our previous study showed recovery and recycling of the core double-shell nanomaterials with an external magnet after two complete cycles (Fig. S7) that was used in the third cycle for biomass conversion, without significant loss of the photocatalytic ability in the third cycle compared to that in the first cycle (data to be presented elsewhere).

Under the same concentration of the two types of the nanomaterials, a higher molar absorptivity over a broad range (e.g., 200 – 700 nm) for rGO loaded nanomaterials compared to the bare nanomaterials indicates that the nanohybrids absorb light better at both UV and visible light ranges, a feature that would provide the nanohybrids with more efficient utilization of light than the bare nanoparticles. Furthermore, the rGO sheets can act as an electron-trap and facilitate transport of photogenerated electrons. This electron conduction throughout the Fe_3O_4@SiO_2@α-Fe_2O_3/TiO_2-rGO photocatalyst can slow the charge-carrier recombination during photocatalysis; thus, this feature can further increase the generation of reactive oxygen species (e.g., hydroxyl radicals) that in turn will enhance the oxidative conversion of lignocellulose under fluorescent light. In our study, photogenerated hydroxyl radicals ·OH were detected using both nanomaterials with and without rGO support under fluorescent light irradiation (Fig. 9). Further, significant higher concentrations of ·OH were produced by rGO-supported nanomaterials compared to the nanomaterials without rGO support during four hours under fluorescent light (Fig. 9). In addition, due to the surfactant nature

of sodium lignosulfonate, supporting Fe_3O_4@SiO_2@α-Fe_2O_3/TiO_2 with a carbonaceous material can further enhance adsorption of sodium lignosulfonate by inducing concomitant metal-sulfonate complexation and carbon-tail interactions. Thus, multipoint and cooperative adsorption of sodium lignosulfonate was enabled on rGO-supported nanomaterials to potentially increase the adsorption of lignocellulose for its conversion (Fig. 8).

4 Conclusion

A hierarchical Fe_3O_4@SiO_2@α-Fe_2O_3/TiO_2 composite photocatalyst was successfully produced in this study with a superparamagnetic Fe_3O_4 nanosphere as the inner center, an inactive SiO_2 layer as the middle layer, and a photoactive α-Fe_2O_3/TiO_2 exterior layer that is responsible for the material's photocatalytic properties under visible light. The core double-shell nanomaterials were further supported with rGO and characterized for their physical and photocurrent properties. VSM, XPS and XRD characterization showed both materials with and without rGO support are soft ferromagnetic and the presence of Fe_3O_4, TiO_2, Fe_2O_3 and SiO_2 in both nanomaterials. The efficient photoactivity of the Fe_3O_4@SiO_2@α-Fe_2O_3/TiO_2-rGO nanohybrids was confirmed for conversion of two lignocellulose model compounds (D-xylose and sodium lignosulfonate to valuable products) under cool white fluorescent light. Moreover, improved transformations were achieved using rGO-supported nanoparticles compared to the bare nanoparticles. It is likely that the rGO support enhanced the efficiency of photogenerated electron capture by the core double-shell nanoparticles, thus reducing the electron/hole pair recombination and increasing the generation of ·OH to promote the conversion of the starting materials to the desired products. As a result of this research, a new method for integrating multifunctional composite photocatalysts with enhanced photocatalytic activity was developed. The method developed herein can also be applied to synthesize other multifunctional nanomaterials. The photocatalytic nanomaterials developed in this study were used to convert a lignocellulosic biomass—Brewer's Spent Grain (BSG) with relatively high conversion efficiency. It is expected that the composite photocatalysts developed in this study will ultimately enable large-scale, energy-efficient, economically and environmentally sustainable operations for heterogeneous photocatalytic transformation of wasted lignocellulosic biomass under visible light to value-added chemicals.

Supplementary Information The online version contains supplementary material available at https://doi.org/10.1007/s13399-023-04280-z.

Authors' contributions Sudip Baral made substantial contributions to the acquisition, analysis, and interpretation of data; drafted the work. Chunjie Xia, Elise Jinon, and Cole Cameron carried out the experiment and collected the data. Ishani M. Senanayake and Haoran Yang carried out the experiments for revising the manuscript to address the comments of the reviewers. Boyd M. Goodson and Yuhong Qin made critical contributions to the presented idea and the final version of the manuscript. Jia Liu made substantial contributions to the conception of the work; supervised the project; revised the work critically for important intellectual content.

Funding This research was supported by the Energy Boost Seed Grant from the Advanced Coal and Energy Research Center, Southern Illinois University Carbondale. B.M.G. and E.J. acknowledge support from NSF (CHE-1905341 and REU funding from the NSF/DoD ASSURE Program, DMR-1757954 and DMR-2150489). Y.H.Q. acknowledges support from the China Scholarship Council (201808140258). The authors acknowledge the use of facilities and instrumentation at the Materials Research Laboratory Central Research Facilities, University of Illinois, partially supported by NSF through the University of Illinois Materials Research Science and Engineering Center DMR-1720633.

Data availability The data and materials that support the findings of this study are available from the corresponding author upon reasonable request.

Declarations

Ethical approval Not applicable.

Competing interests The authors declare that they have no known competing financial interests or personal relationships that could have appeared to influence the work reported in this paper.

References

1. Saini JK, Saini R, Tewari L (2015) Lignocellulosic agriculture wastes as biomass feedstocks for second-generation bioethanol production: concepts and recent developments. 3 Biotech 5(4):337–353
2. Den W, Sharma VK, Lee M, Nadadur G, Varma RS (2018) Lignocellulosic biomass transformations via greener oxidative pretreatment processes: access to energy and value-added chemicals. Front Chem 6:141–141
3. Kumar AK, Sharma S (2017) Recent updates on different methods of pretreatment of lignocellulosic feedstocks: a review. Bioresour Bioprocess 4(1):7–7
4. Izumi Y (2015) Recent Advances (2012–2015) in the Photocatalytic Conversion of Carbon Dioxide to Fuels Using Solar Energy: Feasibilty for a New Energy. In Advances in CO₂ Capture, Sequestration, and Conversion. American Chemical Society, p. 1-46
5. Puga AV (2016) Photocatalytic production of hydrogen from biomass-derived feedstocks. Coord Chem Rev 315:1–66
6. Granone LI, Sieland F, Zheng N, Dillert R, Bahnemann DW (2018) Photocatalytic conversion of biomass into valuable products: a meaningful approach? Green Chem 20(6):1169–1192
7. Caravaca A, Jones W, Hardacre C, Bowker M (2016) H(2) production by the photocatalytic reforming of cellulose and raw biomass using Ni, Pd, Pt and Au on titania. Proc Math Phys Eng Sci 472(2191):20160054–20160054
8. Lombardi E (2013) *Selective photo-oxidation of cellobiose with tio2-supported metal nanoparticles*. The University of Bologna
9. Skillen N, Daly H, Lan L, Aljohani M, Murnaghan CWJ, Fan X, Hardacre C, Sheldrake GN, Robertson PKJ (2022) Photocatalytic

reforming of biomass: what role will the technology play in future energy systems. Top Curr Chem 380(5):33
10. Prado R, Erdocia X, Labidi J (2013) Effect of the photocatalytic activity of TiO_2 on lignin depolymerization. Chemosphere 91(9):1355–1361
11. Chen M, Shen X, Wu Q, Li W, Diao G (2015) Template-assisted synthesis of core–shell α-Fe_2O_3@TiO_2 nanorods and their photocatalytic property. J Mater Sci 50(11):4083–4094
12. He Q, Zhang Z, Xiong J, Xiong Y, Xiao H (2008) A novel biomaterial — Fe_3O_4:TiO_2 core-shell nano particle with magnetic performance and high visible light photocatalytic activity. Opt Mater 31(2):380–384
13. El-Toni AM, Habila MA, Labis JP, Alothman ZA, Alhoshan M, Elzatahry AA, Zhang F (2016) Design, synthesis and applications of core–shell, hollow core, and nanorattle multifunctional nanostructures. Nanoscale 8(5):2510–2531
14. Kim S-K, Day RW, Cahoon JF, Kempa TJ, Song K-D, Park H-G, Lieber CM (2012) Tuning light absorption in core/shell silicon nanowire photovoltaic devices through morphological design. Nano Lett 12(9):4971–4976
15. Mandal S, Chaudhuri K (2016) Engineered magnetic core shell nanoprobes: synthesis and applications to cancer imaging and therapeutics. World J Biol Chem 7(1):158–167
16 Abbas M, Rao BP, Reddy V, Kim C (2014) Fe_3O_4/TiO_2 core/shell nanocubes: Single-batch surfactantless synthesis, characterization and efficient catalysts for methylene blue degradation. Ceram Int 40(7, Part B):11177–11186
17. Abbas N, Shao GN, Imran SM, Haider MS, Kim HT (2016) Inexpensive synthesis of a high-performance Fe_3O_4-SiO_2-TiO_2 photocatalyst: Magnetic recovery and reuse. Front Chem Sci Eng 10(3):405–416
18. Habila MA, Alothman ZA, El-Toni AM, Labis JP, Soylak M (2016) Synthesis and application of Fe_3O_4@SiO_2@TiO_2 for photocatalytic decomposition of organic matrix simultaneously with magnetic solid phase extraction of heavy metals prior to ICP-MS analysis. Talanta 154:539–547
19. Chiang YD, Dutta S, Chen CT, Huang YT, Lin KS, Wu JCS, Suzuki N, Yamauchi Y, Wu KC-W (2015) Functionalized Fe_3O_4@Silica core-shell nanoparticles as microalgae harvester and catalyst for biodiesel production. Chemsuschem 8(5):789–794
20. Mahajan J, Jeevanandam P (2018) Synthesis of TiO_2@α-Fe_2O_3 core–shell heteronanostructures by thermal decomposition approach and their application towards sunlight-driven photodegradation of rhodamine B. New J Chem 42(4):2616–2626
21. Li X, Lin H, Chen X, Niu H, Liu J, Zhang T, Qu F (2016) Dendritic α-Fe_2O_3/TiO_2 nanocomposites with improved visible light photocatalytic activity. Phys Chem Chem Phys 18(13):9176–9185
22. Zhang X, Xie Y, Chen H, Guo J, Meng A, Li C (2014) One-dimensional mesoporous Fe_2O_3@TiO_2 core–shell nanocomposites: Rational design, synthesis and application as high-performance photocatalyst in visible and UV light region. Appl Surf Sci 317:43–48
23. Uzunbayir B, Kartal U, Doluel EC, Yurddaskal M, Erol M (2020) Development of α-Fe_2O_3/TiO_2 3D hierarchical nanostructured photocatalysts through electrochemical anodization and sol–gel methods. J Sol-Gel Sci Technol 96(2):441–451
24. Gomez-Ruiz B, Ribao P, Diban N, Rivero MJ, Ortiz I, Urtiaga A (2018) Photocatalytic degradation and mineralization of perfluorooctanoic acid (PFOA) using a composite TiO_2 −rGO catalyst. J Hazard Mater 344:950–957
25. Li Z, Zhang P, Li J, Shao T, Jin L (2013) Synthesis of In_2O_3-graphene composites and their photocatalytic performance towards perfluorooctanoic acid decomposition. J Photochem Photobiol, A 271:111–116
26. Wang WS, Wang DH, Qu WG, Lu LQ, Xu AW (2012) Large ultrathin anatase TiO2 nanosheets with exposed 001 facets on graphene for enhanced visible light photocatalytic activity. J Phys Chem C 116(37):19893–19901
27. Xu B, Ahmed MB, Zhou JL, Altaee A, Wu M, Xu G (2017) Photocatalytic removal of perfluoroalkyl substances from water and wastewater: Mechanism, kinetics and controlling factors. Chemosphere 189:717–729
28. Etacheri V, Di Valentin C, Schneider J, Bahnemann D, Pillai SC (2015) Visible-light activation of TiO_2 photocatalysts: advances in theory and experiments. J Photochem Photobiol, C 25:1–29
29. Park H, Kim HI, Moon GH, Choi W (2016) Photoinduced charge transfer processes in solar photocatalysis based on modified TiO_2. Energy Environ Sci 9(2):411–433
30. Navakoteswara Rao V, Malu TJ, Cheralathan KK, Sakar M, Pitchaimuthu S, Rodríguez-González V, MamathaKumari M, Shankar MV (2021) Light-driven transformation of biomass into chemicals using photocatalysts – Vistas and challenges. J Environ Manag 284:111983
31. Kang YS, Risbud S, Rabolt JF, Stroeve P (1996) Synthesis and characterization of nanometer-size Fe_3O_4 and γ-Fe_2O_3 particles. Chem Mater 8(9):2209–2211
32. He F, Fan J, Ma D, Zhang L, Leung C, Chan HL (2010) The attachment of Fe_3O_4 nanoparticles to graphene oxide by covalent bonding. Carbon 48(11):3139–3144
33. Thu TV, Sandhu A (2014) Chemical synthesis of Fe_3O_4–graphene oxide nanohybrids as building blocks for magnetic and conductive membranes. Mater Sci Eng B 189:13–20
34. Liu J, Williams PC, Geisler-Lee J, Goodson BM, Fakharifar M, Peiravi M, Chen D, Lightfoot DA, Gemeinhardt ME (2018) Impact of wastewater effluent containing aged nanoparticles and other components on biological activities of the soil microbiome, Arabidopsis plants, and earthworms. Environ Res 164:197–203
35. Liu J, Williams PC, Goodson BM, Geisler-Lee J, Fakharifar M, Gemeinhardt ME (2019) TiO_2 nanoparticles in irrigation water mitigate impacts of aged Ag nanoparticles on soil microorganisms, Arabidopsis thaliana plants, and Eisenia fetida earthworms. Environ Res 172:202–215
36. Campobasso M, Peiravi M, Xia C, Liang Y, Liu J (2020) Effects of combined Ag and ZnO nanoparticles on microbial communities from crab orchard creek, Illinois, USA. J Environ Eng 146(7):04020067
37. Jacobsen SE, Wyman CE (2000) Cellulose and hemicellulose hydrolysis models for application to current and novel pretreatment processes. Appl Biochem Biotechnol 84(1):81–96
38. Gong J, Imbault A, Farnood R (2017) The promoting role of bismuth for the enhanced photocatalytic oxidation of lignin on Pt-TiO_2 under solar light illumination. Appl Catal B 204:296–303
39. Xia C, Qu S, Bhattacharjee L, Lim XE, Yang H, Liu J (2022) Degradation of perfluoroalkyl substances using UV/Fe^0 system with and without the presence of oxygen. Environ Technol:1–12. https://doi.org/10.1080/09593330.2022.2041104
40. Bhattacharjee L, Xia C, Krouse E, Yang H, Liu J (2023) Degradation of 1,4-dioxane by heterogeneous photocatalysis and a photo-Fenton-like process under fluorescent light. Environ Technol:1–48. https://doi.org/10.1080/09593330.2023.2192367
41. Ba-Abbad MM, Benamour A, Ewis D, Mohammad AW, Mahmoudi E (2022) Synthesis of Fe_3O_4 nanoparticles with different shapes through a co-precipitation method and their application. JOM 74(9):3531–3539
42. Tan GL, Lemon MF, French RH (2003) Optical properties and London dispersion forces of amorphous silica determined by vacuum ultraviolet spectroscopy and spectroscopic ellipsometry. J Am Ceram Soc 86(11):1885–1892
43. Makuła P, Pacia M, Macyk W (2018) How to correctly determine the band gap energy of modified semiconductor photocatalysts based on UV–Vis spectra. J Phys Chem Lett 9(23):6814–6817

44. Yang S, Yue W, Huang D, Chen C, Lin H, Yang X (2012) A facile green strategy for rapid reduction of graphene oxide by metallic zinc. RSC Adv 2(23):8827–8832
45. Li Z, Huang Y, Chi X, Li D, Zhong L, Li X, Liu C, Peng X (2022) Biomass-based N doped carbon as metal-free catalyst for selective oxidation of d-xylose into d-xylonic acid. Green Energy Environ 7(6):1310–1317
46. Rohini B, Hebbar HU (2021) Photocatalytic conversion of xylose to xylitol over copper doped zinc oxide catalyst. Catal Lett 151(9):2583–2594
47. Werpy T, Petersen G, Aden A, Bozell J, Holladay J, White J, Manheim A, Elliot D, Lasure L, Jones S, Gerber M, Ibsen K, Lumberg L, Kelley S (2004) Top value added chemicals from biomass, vol I. In: Werpy GPT (ed.) Results of Screening for Potential Candidates from Sugars and Synthesis Gas. U.S. Department of Energy, Energy Efficiency and Renewable Energy
48. Ko BS, Kim J, Kim JH (2006) Production of Xylitol from d-Xylose by a Xylitol Dehydrogenase Gene-Disrupted Mutant of Candida tropicalis. Appl Environ Microbiol 72(6):4207–4213
49. Zhang H, Han X, Wei C, Bao J (2017) Oxidative production of xylonic acid using xylose in distillation stillage of cellulosic ethanol fermentation broth by Gluconobacter oxydans. Biores Technol 224:573–580
50. *CHEBI:22605 - arabinitol*. Chemical Entities of Biological Interest 11 November 2014; Available from: https://www.ebi.ac.uk/chebi/searchId.do?chebiId=CHEBI:22605#:~:text=Arabitol%2C%20or%20arabinitol%2C%20is%20a,or%20other%20yeast%2Ffungus%20species
51. Yankov D (2022) Fermentative lactic acid production from lignocellulosic feedstocks: from source to purified product. Front Chem 10:823005
52. Weng C, Peng X, Han Y (2021) Depolymerization and conversion of lignin to value-added bioproducts by microbial and enzymatic catalysis. Biotechnol Biofuels 14(1):84
53. Qiu J, Dai D, Zhang L, Li M, Xu J, Yao J (2021) Photocatalytic conversion of sodium lignosulfonate into vanillin using mesoporous TiO_2 derived from MIL-125. Microporous Mesoporous Mater 319:111043
54. Wu K, Cao M, Zeng Q, Li X (2023) Radical and (photo)electron transfer induced mechanisms for lignin photo- and electro-catalytic depolymerization. Green Energy Environ 8(2):383–405
55. Dong C, Xing M, Zhang J (2020) Recent progress of photocatalytic fenton-like process for environmental remediation. Front Environ Chem 1. https://doi.org/10.3389/fenvc.2020.00008
56. Kramar A, Anishchenko V, Kuzema P, Smirnova N, Laguta I, Stavinskaya O, Ivannikov R, Linnik O (2022) Features of lignosulfonate depolymerization and photocatalytic transformation to low-molecular-weight compounds over nano-sized semiconductive films. Appl Nanosci 12(8):2345–2355
57. Holladay JEW, James F, Bozell JJ, Johnson D (2007) *Top Value-Added Chemicals from Biomass - Volume II—Results of Screening for Potential Candidates from Biorefinery Lignin.* U.S. Department of Energy, Office of Scientific and Technical Information